#### **Research Article**

Wenjuan Zhang\*, Yuheng Li, Mengyu Ran, Youliang Wang\*, Yezhi Ding, Bobo Zhang, Qiancheng Feng, Qianqian Chu, Yongqian Shen, and Wang Sheng

# Fe nanoparticle-functionalized ordered mesoporous carbon with tailored mesostructures and their applications in magnetic removal of Aq(I)

https://doi.org/10.1515/rams-2024-0007 received November 02, 2023; accepted March 08, 2024

Abstract: Fe nanoparticle-functionalized ordered mesoporous carbon (Fe<sup>0</sup>/OMC) was synthesized using triblock copolymers as templates and through solvent evaporation self-assembly, followed by a carbothermal reduction. Fe<sup>0</sup>/OMC had three microstructures of two-dimensional hexagonal (space group, p6mm, Fe<sup>0</sup>/OMC-1), body centered cubic (Im3m, Fe<sup>0</sup>/OMC-2), and face centered cubic (Fm3m, Fe<sup>0</sup>/OMC-3) which were controlled by simply adjusting the template. All Fe<sup>0</sup>/OMC displayed paramagnetic characteristics, with a maximum saturation magnetization of 50.1 emu·g<sup>-1</sup>. This high magnetization is advantageous for the swift extraction of the adsorbent from the solution following the adsorption process. Fe<sup>0</sup>/OMC was used as an adsorbent for the removal of silver ions (Ag(1)) from aqueous solutions, and the adsorption capacity of Fe<sup>0</sup>/OMC-1 was enhanced by the functionalization of Fe<sup>0</sup>. Adsorption property of Fe<sup>0</sup>/ OMC-1 was significantly higher than that of Fe<sup>0</sup>/OMC-2 and Fe<sup>0</sup>/OMC-3, indicating that the long and straight ordered pore channels were more favorable for adsorption, and the adsorption capacity of Ag(1) on Fe<sup>0</sup>/OMC-1

Yuheng Li, Mengyu Ran, Yezhi Ding, Bobo Zhang, Qiancheng Feng: School of Materials Science and Engineering, Lanzhou University of Technology, Gansu, Lanzhou, 730050, China

**Qianqian Chu, Yongqian Shen, Wang Sheng:** State Key Laboratory for Advanced Processing and Recycling of Non-ferrous Metals, Lanzhou University of Technology, Gansu, Lanzhou, 730050, China; School of Materials Science and Engineering, Lanzhou University of Technology, Gansu, Lanzhou, 730050, China

was 233 mg·g<sup>-1</sup>. The adsorption process exhibited conformity with both the pseudo-second-order kinetic model and the Freundlich model, suggesting that the dominant mechanism of adsorption involved multilayer adsorption on heterogeneous surfaces.

**Keywords:** Fe, ordered mesoporous carbon, Ag(I), adsorption

## 1 Introduction

As industrialization has progressed, the pollution resulting from heavy metal wastewater has become increasingly severe. The presence of heavy metals ions in the environment poses a threat to both the ecosystem and human health [1,2]. Nowadays, the problem of water pollution has been paid more and more attention by the researchers and the general public because of its potential threat to human existence. Particularly, heavy metal ions are considered as one of the biggest challenges for environmentalists due to its high toxic and non-biodegradable nature. Moreover, they may accumulate in the body through the food chain, which is harmful to the ecosystem and human health. Therefore, it is very important to find a suitable method for the removal of such toxic metal ions from the waste water [3]. Silver is recognized as one of the most significant heavy metals. Silver, with its exceptional electrical and thermal conductivity, outperforms other metals in these aspects. It also exhibits superior resistance to corrosion and oxidation, making it highly desirable for various applications. Due to these characteristics, silver found extensive application in various industrial sectors, including the manufacturing of mirrors, photographic films, batteries, and electronic devices [4]. Nevertheless, it is important to note that silver is also recognized as a potentially toxic substance, and high concentrations of silver can lead to adverse health effects, such as liver and kidney degeneration, as well

<sup>\*</sup> Corresponding author: Wenjuan Zhang, State Key Laboratory for Advanced Processing and Recycling of Non-ferrous Metals, Lanzhou University of Technology, Gansu, Lanzhou, 730050, China, e-mail: wenjuanzhang86@163.com

<sup>\*</sup> Corresponding author: Youliang Wang, School of Mechanical and Electrical Engineering, Lanzhou University of Technology, Gansu, Lanzhou, 730050, China, e-mail: wangyouliang20@163.com

as respiratory disorders [5]. The toxicity of silver, combined with its significant economic value, has created a demand for a treatment method that can effectively remove this metal from wastewater while also recovering the valuable material. This approach aims to prevent ecological destruction and promote sustainable practices. Many methods of removing heavy metal have been reported, including precipitation, oxidation, membrane filtration, reduction, ion exchange, and adsorption [6]. Among these different methods, adsorption method had proven to be an effective and economical treatment process [7].

Herman et al. prepared mercapto-functionalized porous silica particles using (3-mercaptopropyl)-trimethoxysilane co-gelation, and the resulting short-range ordered porous silica particles were particularly effective adsorbents for aqueous-phase silver ions (Ag(I)). The binding of Ag(I) in aqueous solution was almost stoichiometric over a wide range of pH 4.0-9.0, even at lower Ag(1) concentrations, until the limiting adsorption amount of 238 mg g<sup>-1</sup> was reached. Furthermore, washing with 10 mM Na<sub>2</sub>S<sub>2</sub>O<sub>3</sub> solution resulted in almost complete recovery of Ag(1) and regeneration of the adsorbent [8]. Al-Anber et al. successfully loaded (Ag(1)) onto a specially functionalized silica matrix, termed SG-Cys-Na<sup>+</sup>, by batch sorption technique utilizing cysteine-functionalized silica (SG-Cys-Na<sup>+</sup>) against fully loaded Ag(i). And under certain conditions, an impressive 98% loading efficiency was obtained. This chemisorption involves strong chemical bonding between the Ag(i) and the carboxylate groups (-COO-Na<sup>+</sup>) of functionalized silica gel. Valuable insights into the potential application of SG-Cys-Na<sup>+</sup> matrix as a highly efficient filtration of Ag(1) from aqueous solutions were provided [9]. Fan et al. prepared passion fruit shell source s-doped porous carbon (SPC) by hydrothermal carbonization and KOH/(NH<sub>4</sub>)<sub>2</sub>SO<sub>4</sub> activation. The optimized SPC-3 showed a maximum adsorption of Ag(1) up to 115 mg·g<sup>-1</sup> in 0.5 mol·L<sup>-1</sup> HNO<sub>3</sub> solution. SPC-3 showed good selectivity for a variety of competing cations, Ag(1), which was mainly attributed to the formation of Ag<sub>2</sub>S nanoparticles due to the strong bonding between the Ag(I) ions and the sulfurcontaining functional groups on the surface of SPC-3 [10].

Nanoscale zero valent iron (nZVI, Fe<sup>0</sup>) was an environmental-friendly nanomaterial with great magnetic properties and high specific surface area. Fe<sup>0</sup> nanoparticles were highly beneficial for adsorptive removal of silver. Fe<sup>0</sup> nanoparticles were a strong reductant due to the low standard redox potential ( $E^6 = -0.44 \,\mathrm{V}$ ) of Fe<sup>2+</sup>/Fe<sup>0</sup> couple [11,12]. Fe<sup>0</sup> displayed great potential in the removal of environmental contaminants such as trichloroethylene, chlorinated methane, polybrominated diphenyl ethers, nitroaromatics, nitrate, and heavy metal ions. Fe<sup>0</sup> nanoparticles have demonstrated a versatile ability to reduce

heavy metals present in wastewater. The mechanisms of heavy metal removal by Fe<sup>0</sup> nanoparticles involves reduction, adsorption, and co-precipitation [13]. These combined processes effectively facilitate the removal of heavy metals from wastewater. Consequently, the utilization of Fe<sup>0</sup> as a reducing agent offers a simple and convenient method to mitigate heavy metal pollution in wastewater. However, the use of Fe<sup>0</sup> nanoparticles alone to remove contaminants from water might not be very effective for the following reasons: 1) Fe<sup>0</sup> nanoparticles show a high tendency to agglomerate because of the magnetic forces, gravitational forces, and high interfacial energies, resulting in reduced surface area and reactivity. 2) The environmental exposure of bare Fe<sup>0</sup> nanoparticles was found to be unstable, posing significant challenges for the practical application of environmental remediation [14].

In order to overcome these problems, fixing the Fe<sup>0</sup> nanoparticles in or on the supports could provide sufficient loading sites for the immobilization of Fe<sup>0</sup> nanoparticles preventing them from being oxidized and agglomerated. Various supports, such as amorphous activated carbon, molecular sieves, polymers, etc., [15,16] had been reported as supports to protect Fe<sup>0</sup> nanoparticles from agglomeration and oxidation. However, these approaches might inhibit the reaction of Fe<sup>0</sup> nanoparticles with pollutants or endow Fe<sup>0</sup> nanoparticles with undesirable properties for environmental remediation. Immobilization of Fe<sup>0</sup> nanoparticles in porous carbon had been considered to improve their dispersibility and reactivity [17-19]. Mesoporous carbon materials were considered to be an available support due to their great physicochemical properties. Serving as the support for Fe<sup>0</sup>, mesoporous carbon had a large specific surface area and thermal stability, which could provide excellent adsorption properties. In addition, the mesoporous carbon could effectively control the size of Fe<sup>0</sup> nanoparticles. Lin and Chen successfully synthesized mesoporous Fe/carbon aerogel and employed it for the adsorption of arsenic ions. The maximum adsorption capacity for arsenic ions was found to be 216.9 mg·g<sup>-1</sup> [20]. Fixing Fe<sup>0</sup> nanoparticles in mesoporous carbon effectively elevated the adsorption performance of Fe<sup>0</sup> nanoparticles. But the mesoporous carbon was associated with certain drawbacks, such as the disordered and collapsed structure that might block the pore channels [21]. To begin with, porous carbon materials with a porous structure could effectively prevent the agglomeration of iron nanoparticles by confining and dispersing them. Furthermore, the distinctive surface properties and electronic properties of carbon materials contribute positively to charge transfer and accumulate Ag(1). Finally, carbon materials had the high stability in acid and alkali environments, which were very important for the regeneration of the adsorbent and the recovery of Ag(1) [22].

Recently, high-ordered mesoporous carbon materials (OMC) with large surface area and high porosity have been reported, as a kind of multifunctional nanomaterial, it has great potential in the fields of catalysis, adsorption and separation, hydrogen and methane storage, supercapacitor, and so on [23].

The Pt-OMC catalysts synthesized by Liu et al. exhibited superior electrocatalytic properties in the oxygen reduction reaction when compared to typical commercial electrocatalysts. This indicates that Pt-OMC holds great potential as an efficient and effective catalyst for electrochemical processes, offering improved performance and enhanced catalytic activity [24]. Li et al. successfully synthesized biomass derived ordered mesoporous carbon (BOMC) materials, which exhibited a high Brunauer-Emmett-Teller (BET) surface area of 1,385 m<sup>2</sup>·g<sup>-1</sup>. In addition, they also prepared iron-impregnated BOMC (Fe/BOMC) materials with a slightly reduced BET surface area of 1,012  $\mathrm{m}^2 \cdot \mathrm{g}^{-1}$ . These materials with their large surface areas offer a significant amount of active sites for adsorption and catalytic applications, making them promising candidates for various environmental and energy-related applications. These materials were employed for the adsorption of Pb(II) and Cr(III) [25]. The presence of a considerable number of mesopores within iron-impregnated BOMC (Fe/BOMC) enhances the diffusion of metal ions. This structural characteristic allows for efficient uptake of metal contaminants from solution. In the case of Fe/BOMC, the maximum adsorption capacity for Pb(II) was determined to be 123 mg·g<sup>-1</sup>, while for Cr(III), it was found to be 46 mg·g<sup>-1</sup>. These values indicate the high adsorption efficiency of Fe/BOMC in removing these heavy metal ions from wastewater, highlighting its potential for environmental remediation applications. Consequently, OMC has demonstrated significant potential as a support material for nanoparticles, primarily due to its numerous advantages in the adsorption and delivery of heavy metal ions. The BET surface areas of mesoporous carbon did not completely determine the adsorption and separation property of the materials, and their mesostructures had an excellent influence on the transfer and adsorption of pollutants. The various porous structures showed not only the different transport capacities but also the different load forms of metals, including dispersion on the surface of the material and filling into the inside of the pores. However, studies on the transport capacity and adsorption properties of the porous structure of Fe<sup>0</sup>/OMC for metal ions were lacking. OMC materials had been synthesized with various porous structures, which could be attributed to the use of different raw materials and synthetic methods. Depending on the specific combination of precursors and synthesis conditions, OMC could exhibit diverse porous structures, including two-dimensional hexagonal, threedimensional cubic, lamellar, and more. These distinct structures contribute to the unique properties and applications of OMC materials, allowing for tailoring their characteristics to specific needs in various fields such as adsorption, catalysis, and energy storage [26].

In this work, Fe<sup>0</sup>/OMC was prepared through a twostep synthesis that involved the formation of OMC by using triblock copolymers as templates and through a solvent evaporation self-assembly approach, followed by a carbothermal reduction of Fe<sup>3+</sup> solutions at high temperatures under Ar atmosphere to form Fe<sup>0</sup>/OMC. The surface morphology, chemical composition, and magnetic properties of the Fe<sup>0</sup>/OMC were characterized and extensive investigation of the adsorption capacity of Ag(I) on Fe<sup>0</sup>/OMC in agueous solutions were performed.

## 2 Materials and methods

#### 2.1 Materials

Triblock poly(ethylene oxide)-b-poly(propylene oxide)-bpoly(ethylene oxide) copolymer Pluronic F127 (PEO<sub>106</sub>PPO<sub>70</sub> PEO<sub>106</sub>) and diblock poly(ethylene oxide)-b-poly(styrene) copolymer (PEO<sub>100</sub>-PS<sub>114</sub>) were purchased from Aldrich. Phenol, formaldehyde, sodium hydroxide, hydrochloric acid, ferric chloride hexahydrate (FeCl<sub>3</sub>·6H<sub>2</sub>O), ethanol, silver nitrate, potassium periodate (KIO<sub>4</sub>), and potassium persulfate (K<sub>2</sub>S<sub>2</sub>O<sub>8</sub>) were obtained from Tianjin Chemical. All reagents were used as received without further purification.

#### 2.2 Synthesis of OMC

OMC was prepared according to the method reported by Zhao et al. [27,28]. In a typical synthesis procedure, 6.1 g of phenol was melted at 40°C. Subsequently, 1.3 g of 20 wt% NaOH was slowly added to the melted phenol with continuous stirring. Following the dropwise addition of 10.5 g of 37 wt% formaldehyde solution, the reaction mixture was stirred at 70°C for 1h. Once the mixture cooled to room temperature, the pH was adjusted to neutral using a 0.6 M HCl solution. The resulting mixture was then subjected to rotational evaporator for 2 h at 45°C to obtain a viscous liquid. The final sample was re-dissolved in ethanol to form a 20 wt% ethanol solution.

To obtain OMC-1 and OMC-2 the following steps were followed. First, 1.0 g of F127 was dissolved in ethanol to form a homogeneous solution. Then, solutions containing 5.0 or 10.0 g of ethanol was added dropwise to the mixture while stirring for 30 min. The resulting solution was transferred to an evaporating dish and left to evaporate at room temperature overnight, resulting in the formation of a transparent film. This film was then heated in an oven at 100°C for 24 h to thermopolymerize the phenolic resins in the film. Finally, the products were carbonized by heating them at a rate of 5 °C·min<sup>-1</sup> under an Ar atmosphere, reaching a temperature of 800°C and maintaining it for 2 h. These samples were named OMC-1 and OMC-2, respectively.

 $0.1\,\mathrm{g}$  PEO<sub>100</sub>-PS<sub>114</sub> was dissolved in 4.9 g of tetrahydrofuran solution and stirred well, and then  $0.4\,\mathrm{g}$  phenolic resin was dissolved in 1.6 g tetrahydrofuran solution. The two solutions that had been mixed were stirred for 30 min to form a homogeneous solution. The following procedure was similar to that for the synthesis of OMC-1. The obtained sample was named OMC-3.

# 2.3 Synthesis of Fe<sup>0</sup>/OMC

Fe<sup>0</sup>/OMC was synthesized using the incipient wetness impregnation and carbothermic reduction. The synthesis procedure involved the following steps:

 $0.375~g~FeCl_3\cdot 6H_2O$  was dissolved into a small amount of ultrapure water. Then, OMC was added to the previous FeCl<sub>3</sub> solution and stirred for 2 h at room temperature. The obtained black precipitates were cleaned and dried in an oven at 50°C for 24 h. Finally, the black precipitates were carbonized in a tube furnace at 900°C for 2 h under an Ar atmosphere. This synthesis method allowed for the preparation of Fe<sup>0</sup>/OMC composites with different OMC, denoted by the sample names Fe<sup>0</sup>/OMC-1, Fe<sup>0</sup>/OMC-2, and Fe<sup>0</sup>/OMC-3.

#### 2.4 Characterization

The phase composition and ordered intensity of  $Fe^0/OMC$  were analyzed using small-angle X-ray scattering (SAXS) with SAXSess  $mc^2$  mode. Additionally, wide-angle XRD (Rigaku D/max2600) was performed under the conditions of Cu K $\alpha$  radiation, with a current of 100 mA and a voltage of 40 kV. The morphology and mesostructure of  $Fe^0/OMC$  were investigated by TEM (FEI, Tecnai TF20). The specific surface area of the sample was determined by the BET

(Micromeritics ASAP 2460) method, which involves analyzing the  $N_2$  adsorption-desorption isotherm at a temperature of 77 K. The pore volume and pore size distribution were calculated using the BJH method. Additionally, the functional groups presenting on the surface of the sample were examined using Fourier transform infrared (FTIR, NICOLET iS10) spectroscopy. FTIR samples were mixed with dried KBr and pressed as pellets prior to the collection of spectra that covered wave numbers from 500 to 4,000 cm $^{-1}$ . The magnetic properties of Fe $^0$ /OMC were analyzed using a vibration sample magnetometer (VSM, Lakeshore, 7407-S). The magnetic field strength was measured within a range of  $^{-1}$ .5 to 1.5 T to characterize the magnetization behavior of the Fe $^0$ /OMC sample.

#### 2.5 Adsorption experiments of Aq(I)

The adsorption performance of  $Fe^0/OMC$  on Ag(i) in an aqueous solution was investigated using the static adsorption method. A concentration of  $1\,g^{-1}$  of Ag(i) was prepared by dissolving a specific quantity of  $AgNO_3$  in ultrapure water. To prepare different concentrations of Ag(i), the stock solution was diluted accordingly. A  $0.0625~mol^{-1}$  KIO<sub>4</sub> solution and a  $2~wt\%~K_2S_2O_8$  solution were utilized as chromogenic agents for Ag(i). The absorbance of the solution was measured at a wavelength of 365~nm using a UV-Vis spectrophotometer. The concentration of Ag(i) was calculated from the standard curve of Ag(i).

The batch experiments for the adsorption of Ag(t) were conducted in a 250 mL sealed conical flask. In each experiment, 10 mg  $Fe^0/OMC$  was added to the flask along with 50 mL of Ag(t) solution at different initial concentrations. The mixture was sonicated and dispersed for 30 min and then placed in a constant temperature oscillator at 298 K and 120 rpm for 24 h.

The aim of the experiments was to investigate the effects of the initial concentration of Ag(1) and the adsorption time on the adsorption capacity of Fe $^0$ /OMC. The initial concentration of Ag(1) solution ranged from 10 to 100 mg·L $^{-1}$ , and the adsorption time varied from 0 to 24 h.

The equilibrium adsorption capacity of Ag(1) and the removal rate were determined using Eqs. (1) and (2), respectively. These equations provide quantitative measures of the amount of Ag(1) adsorbed onto  $Fe^0/OMC$  and the efficiency of Ag(1) removal.

$$Q_{\rm e} = \frac{(C_0 - C_{\rm e})V}{m},\tag{1}$$

$$R = \frac{(C_0 - C_e)}{C_0} \times 100\%. \tag{2}$$

These equations allow for the calculation of the equilibrium adsorption capacity ( $Q_e$ ) and the removal rate (R) of Ag(1) by Fe<sup>0</sup>/OMC. The equilibrium adsorption capacity represents the amount of Ag(1) adsorbed per unit mass of Fe<sup>0</sup>/OMC at equilibrium. The removal rate indicates the percentage of Ag(1) removed from the initial concentration in the solution.

#### 3 Results and discussion

## 3.1 Structures and morphologies of OMC

OMC was synthesized by a facile solvent evaporation induced self-assembly (EISA) strategy with resol as a carbon source (Scheme 1). SAXS patterns were investigated to verify the successful synthesis of OMC with tailored mesostructure as shown in Figure 1. OMC-1 showed two legible diffraction peaks that could correspond to the (10) and (11) planes of the two-dimensional hexagonal (p6mm) structure. The three diffraction peaks in the SAXS patterns of OMC-2 could correspond to the (110), (200), and (211) planes, associated with the body-centered cubic (Im3m) structure. Three diffraction peaks in the SAXS patterns of OMC-3 could also be indexed as (111), (220), and (331) planes, indicating that OMC-3 had an face-centered cubic (Fm3m) structure. OMC possessed the highly ordered arrangements of mesopores.

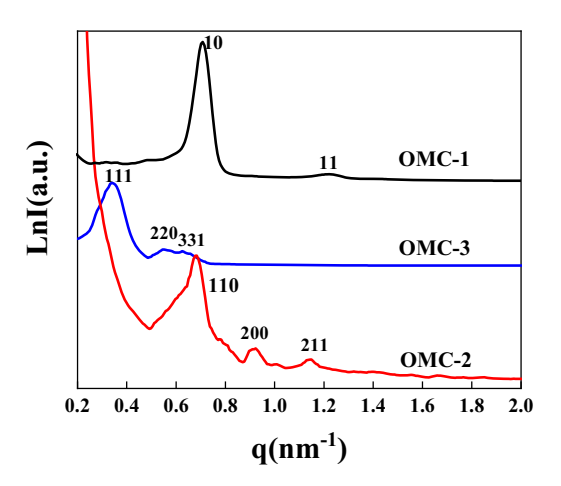
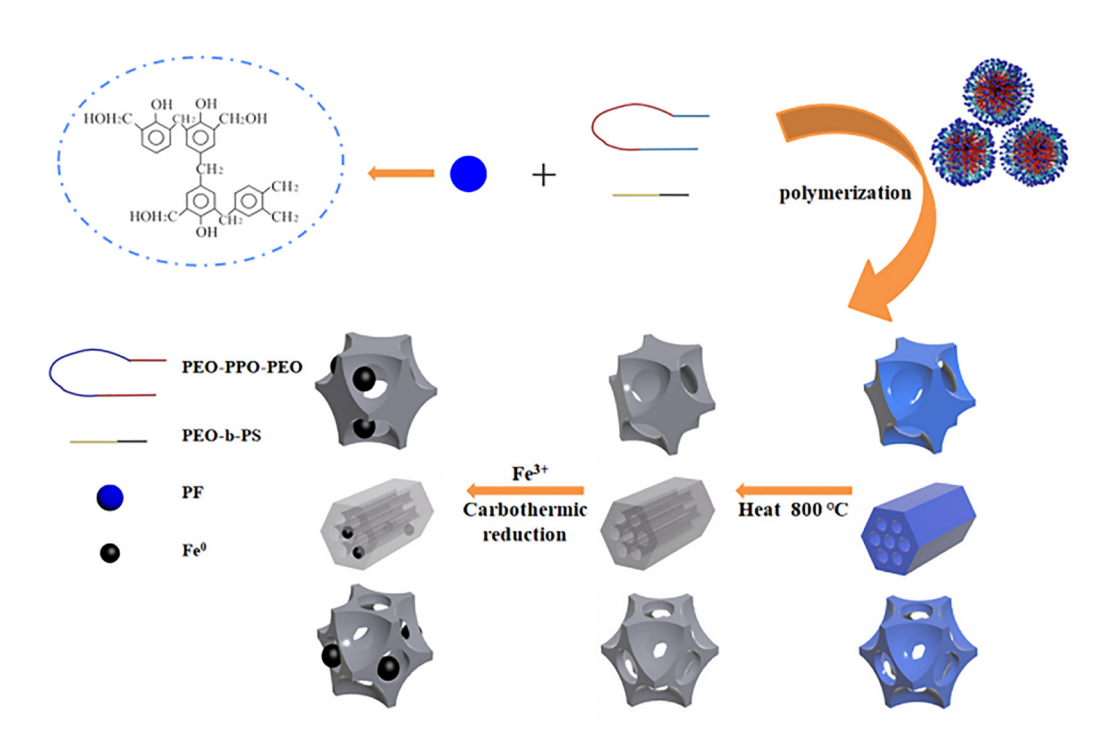


Figure 1: SAXS patterns of OMC.

Figure 2 shows TEM images of OMC-1 viewed along the [001] and [110] directions, OMC-2 viewed along the [111] and [110] directions, and OMC-3 viewed along the [111] and [110] directions. The regular arrangement of the pore channels show that the synthesized OMC-1, OMC-2, and OMC-3 had highly ordered and homogeneous pore channel structures. The observed structures of the samples, namely, the well-ordered two-dimensional hexagonal and body-centered cubic and face-centered cubic mesoporous structures, are consistent with the results obtained from the SAXS patterns. These further demonstrate that OMC with three mesoporous structures were successfully obtained.



Scheme 1: Synthetic route of Fe nanoparticle-functionalized mesoporous carbon with tailored mesostructure.

6 — Wenjuan Zhang et al. DE GRUYTER

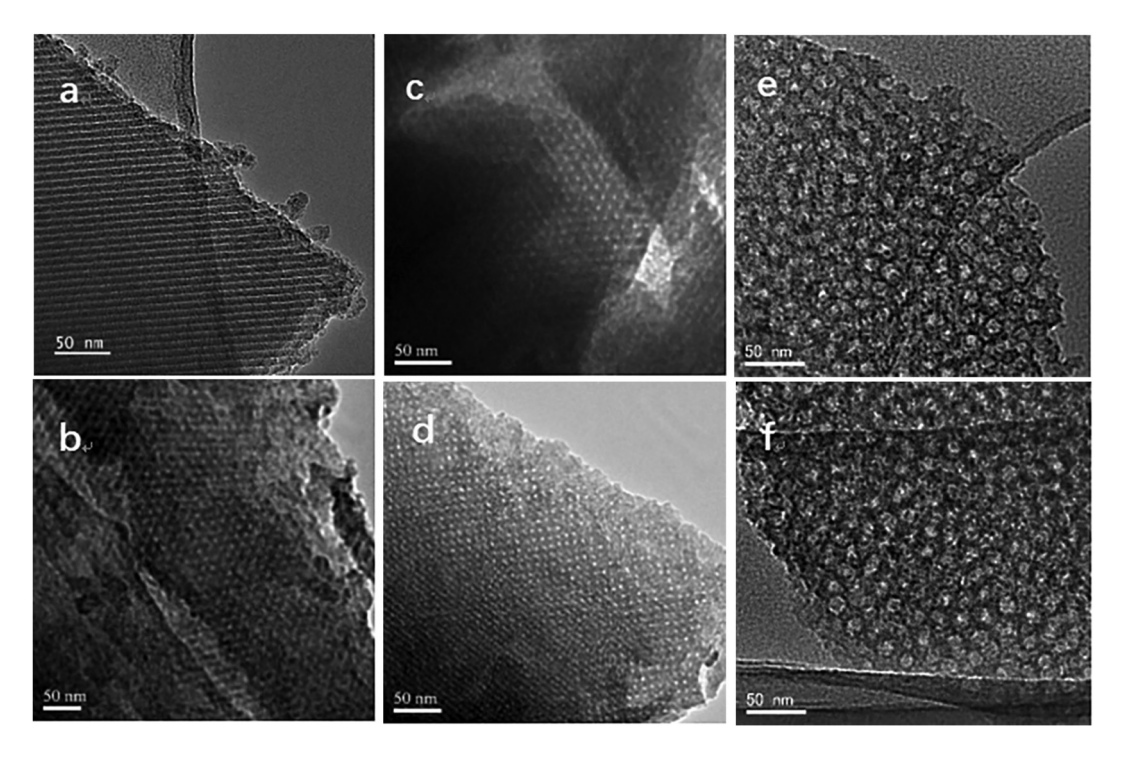
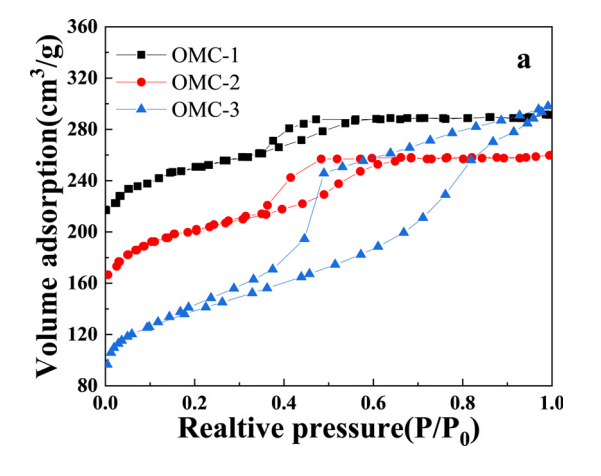


Figure 2: TEM images of OMC-1 viewed along the [001] (a) and [110] (b) directions, OMC-2 viewed along the [111] (c) and [110] (d) directions, and OMC-3 viewed along the [111] (e) and [110] (f) directions.



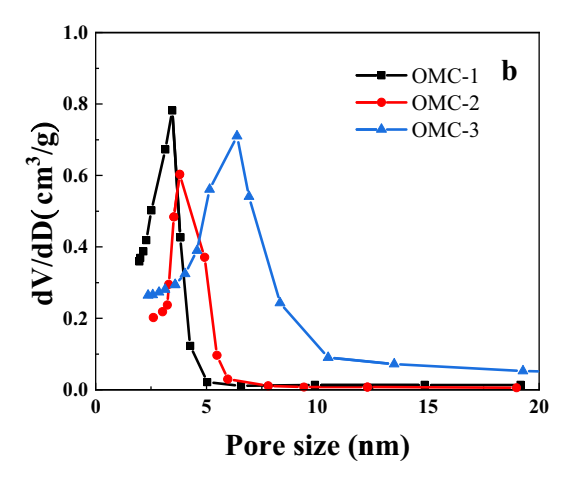


Figure 3: Nitrogen adsorption/desorption isotherms (a) and pore size distribution (b) of OMC.

In order to analyze the pore structures of OMC, the  $\rm N_2$  adsorption-desorption isotherms of  $\rm N_2$  were conducted. Figure 3 shows the isotherms of OMC, which exhibit type IV adsorption isotherms according to the classification defined by the International Union of Pure and Applied Chemistry (IUPAC). These isotherms display an evident H1-type hysteresis loop, with a smooth increase in the medium pressure range ( $P/P_0 = 0.3-0.8$ ), indicating the presence of regularly arranged mesopores.

Table 1 presents the specific surface area and pore volume of OMC samples. OMC-1 exhibits relatively high specific surface area

(649 m²·g⁻¹) and pore volume (0.32 cm³·g⁻¹); OMC-2 and OMC-3 show hysteresis rings in the same relative pressure range, suggesting similar pore structures, but their specific surface areas are lower than that of OMC-1.

# 3.2 Structures and morphologies of Fe<sup>0</sup>/OMC

The WAXS patterns of OMC and Fe<sup>0</sup>/OMC are shown in Figure 4(a). In the case of Fe<sup>0</sup>/OMC, all three types of Fe<sup>0</sup>/OMC exhibited three distinct sharp peaks at 44.2°, 65.0°,

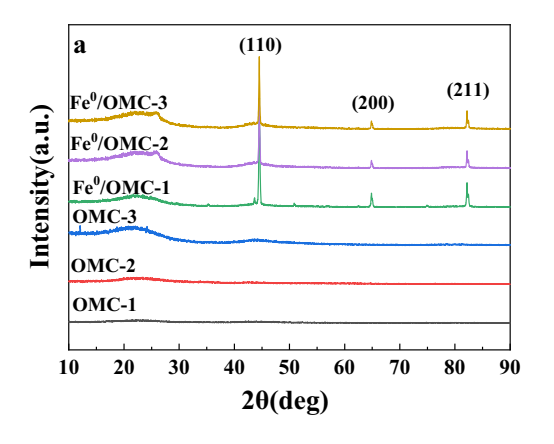
Table 1: Structure and pore properties of OMC

Sample	BET surface area (m²·g <sup>-1</sup> )	Pore volume (cm³·g <sup>-1</sup> )	t-Plot micropore volume (cm³·g <sup>-1</sup> )	Pore size (nm)
OMC-1	676	0.54	0.25	3.4
OMC-2	481	0.40	0.12	3.7
OMC-3	627	0.56	0.28	6.4

and 82.3°, which corresponded to the (110), (200), and (211) crystallographic planes, respectively. These diffraction patterns are consistent with the body-centered cubic  $\alpha$ -Fe structure (JCPDS No. 06-0696). Based on these findings, it is suggested that the presence of OMC acts as a protective agent, helping to prevent the oxidation of Fe<sup>0</sup> and allowing for a greater amount of Fe<sup>0</sup> to be preserved in the material. SAXS patterns of Fe<sup>0</sup>/OMC are shown in Figure 4(b). Similar to the SAXS patterns of Fe<sup>0</sup>/OMC, the intensity of diffraction peak of Fe<sup>0</sup>/OMC only decreased slightly, due to the impregnation of

Fe<sup>0</sup> nanoparticles. This suggested that the regularity of mesostructure of OMC is still maintained after the loading of Fe<sup>0</sup> nanoparticles.

The  $N_2$  adsorption-desorption isotherms were measured to elucidate the mesoporous structures of various  $Fe^0/OMC$ . Figure 5 shows that  $Fe^0/OMC$  has the type IV adsorption isotherms defined by the IUPAC, with an obvious  $H_2$ -type hysteresis loop, and a smooth rise in the medium pressure region ( $P/P_0 = 0.4$ –0.7), which indicated the presence of regularly arranged mesopores. Comparing Table 2



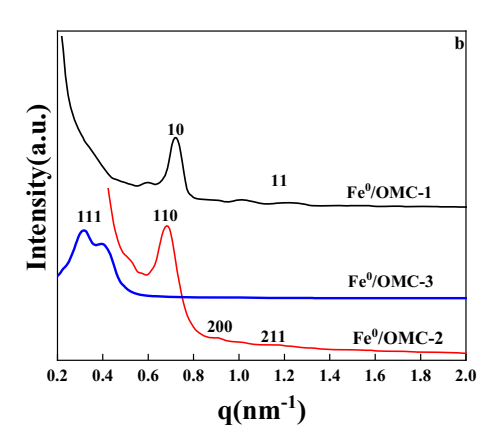
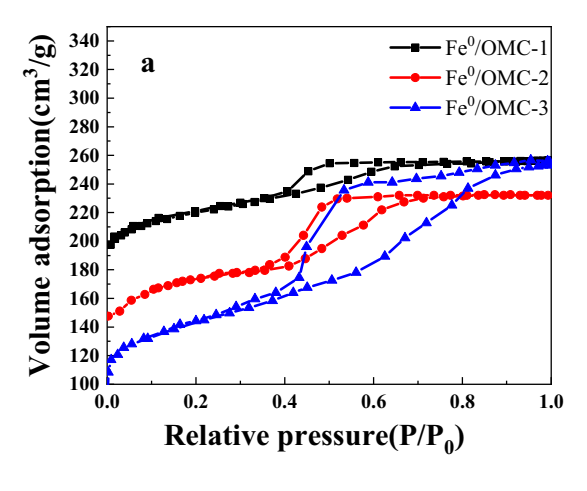


Figure 4: Wide angle X-ray scattering (WAXS) patterns (a) of OMC and Fe<sup>0</sup>/OMC; SAXS patterns of Fe<sup>0</sup>/OMC (b).



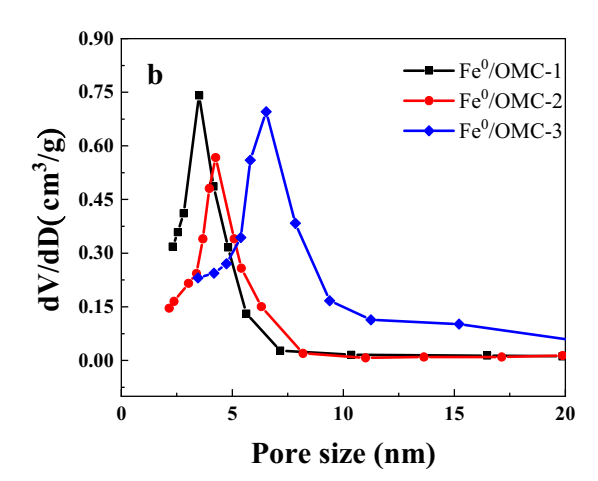


Figure 5: Nitrogen adsorption/desorption isotherms (a) and pore size distribution (b) of Fe<sup>0</sup>/OMC.

8 — Wenjuan Zhang et al. DE GRUYTER

Table 2: Structure and pore properties of Fe<sup>0</sup>/OMC

Sample	BET surface area (m²⋅g <sup>-1</sup> )	Pore volume (cm³·g <sup>-1</sup> )	t-Plot micropore volume (cm³·g <sup>-1</sup> )	Pore size (nm)
Fe <sup>0</sup> /OMC-1	583	0.49	0.21	3.5
Fe <sup>0</sup> /OMC-2	397	0.33	0.10	4.2
Fe <sup>0</sup> /OMC-3	542	0.43	0.20	6.5

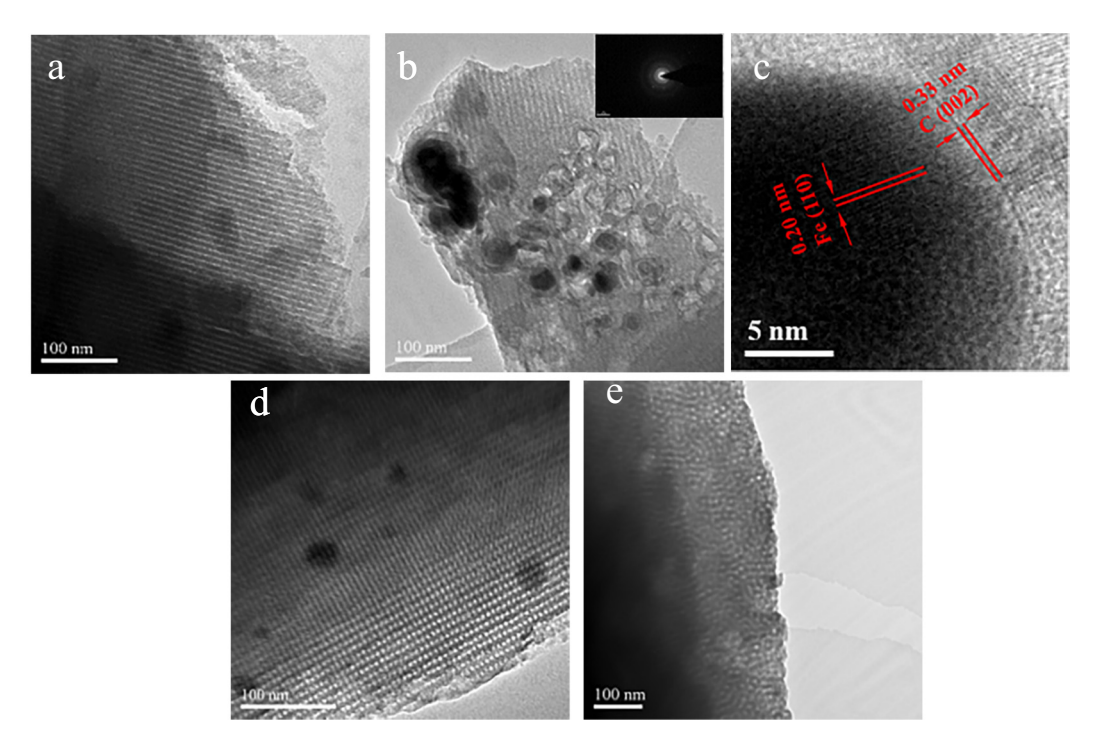
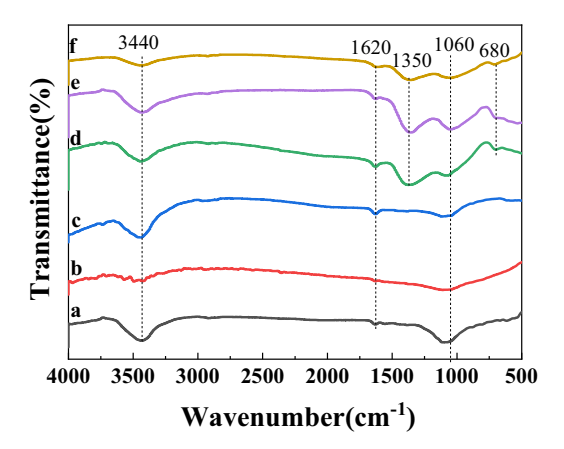


Figure 6: TEM images of OMC-1 (a), Fe<sup>0</sup>/OMC-1 (b), and HRTEM images of Fe<sup>0</sup>/OMC-1 (c). TEM images of Fe<sup>0</sup>/OMC-2 (d) and Fe<sup>0</sup>/OMC-3 (e).

with Table 1, the specific surface area and pore volume decreased after the loading of Fe<sup>0</sup> nanoparticles. Notably, the pore size was basically unchanged because the pore structure was destroyed during the synthesis of Fe<sup>0</sup> nanoparticles, rather than expanding the pore size.

The TEM and HRTEM images of Fe<sup>0</sup>/OMC are shown in Figure 6. The pore structure of OMC-1 could be seen and the dark spots are uniformly embedded in the walls of the OMC (Figure 6(b)). Combining with the lattice stripes in Figure 6(c) and comparing the PDF cards, we could conclude that the black particles were Fe<sup>0</sup>. The HRTEM image of Fe<sup>0</sup> nanoparticles embedded in the wall of OMC illustrated the perfect arrangements of atomic layers and lack of defects. And the lamellar structures on the surface were crystallized graphitic carbon. During the synthesis process, the pores of the ordered mesoporous carbon were partially destroyed, and the collapsed carbon skeleton was crystallized on the surface of the Fe<sup>0</sup> to form a layer of graphitic carbon covering the surface of Fe<sup>0</sup> nanoparticles.

Fourier analyses of different OMC and Fe<sup>0</sup>/OMC were conducted, as depicted in Figure 7. The infrared spectra of the three OMC and Fe<sup>0</sup>/OMC exhibited comparable absorption peaks, indicating that the functional groups presented on their surfaces were similar. Furthermore, the presence of only a few functional groups on the surface can be attributed to the high-temperature calcination process carried out in an argon atmosphere. This suggests that Fe<sup>0</sup>/OMC exists as a pure carbon skeleton with the same composition as OMC, devoid of additional functional groups. The infrared spectra exhibited a prominent absorption peak between 3,300–3,600 cm<sup>-1</sup>, which corresponds to the stretching vibration of O-H bonds. This indicates the presence of a significant number of hydroxyl groups on the surface of the material [29]. Between 1,500 and 1,700 cm<sup>-1</sup> was the stretching vibration peak of C=C. The peak near 1,350 cm<sup>-1</sup> was Fe characteristic absorption peak [30]. The peak observed around 1,060 cm<sup>-1</sup> can be attributed to the stretching vibration of the C-O bond. Additionally, the peak observed near



**Figure 7:** Fourier infrared spectrum of OMC-1 (a), OMC-2 (b), OMC-3 (c), Fe<sup>0</sup>/OMC-1 (d), Fe<sup>0</sup>/OMC-2 (e), and Fe<sup>0</sup>/OMC-3 (f).

680 cm<sup>-1</sup> corresponds to the stretching vibration of Fe–O bonds, indicating the presence of iron (Fe) in the Fe<sup>0</sup>/OMC material [31].

## 3.3 Magnetic behavior of Fe<sup>0</sup>/OMC

To study the magnetic properties of Fe $^0$ /OMC, a series of hysteresis lines were obtained by using the VSM to characterize the magnetic properties as shown in Figure 8, and the magnetic parameters are shown in Table 3. It was concluded that the hysteresis loops of all samples were S-shaped and the saturation magnetization of Fe $^0$ /OMC-1, Fe $^0$ /OMC-2, and Fe $^0$ /OMC-3 were 50.1, 45.8, and 47.7 emu·g $^{-1}$ , respectively, which were all significantly lower than that of Fe $^0$  (142 emu·g $^{-1}$ ). The presence of carbon and the smaller size of Fe $^0$  nanoparticles can be attributed to the lower

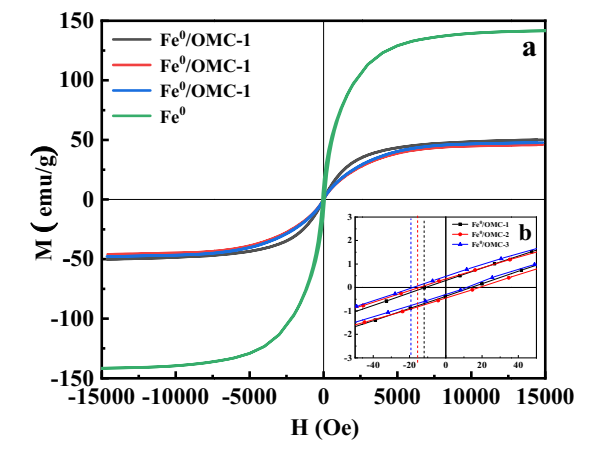




**Figure 8:** Magnetic hysteresis loops of various Fe<sup>0</sup>/OMC and Fe<sup>0</sup> (a) and local enlargement (b) and digital photographs of Fe<sup>0</sup>/OMC under external magnetic field (c).

Table 3: Magnetic properties of Fe<sup>0</sup>/OMC and Fe<sup>0</sup> composites

Samples	Ms (emu∙g <sup>–1</sup> )	Mr (emu∙g <sup>–1</sup> )	Mr/Ms	Hc (Oe)
Fe <sup>0</sup> /OMC-1	50.1	0.35	0.007	15.0
Fe <sup>0</sup> /OMC-2	45.8	0.29	0.006	11.1
Fe <sup>0</sup> /OMC-3	47.7	0.33	0.007	12.2
Fe <sup>0</sup>	143.3	9.66	0.067	70.06

saturation magnetization observed in the  $Fe^0$ /OMC material. The value of Mr/Ms was much less than 0.5, indicating the presence of uniaxial anisotropy in the growth of the magnetic particles. When  $Fe^0$ /OMC particles were dispersed in a solution and exposed to a magnetic field, they exhibited complete separation from the solution, as depicted in the digital photograph of  $Fe^0$ /OMC. This photograph serves as evidence that  $Fe^0$ /OMC displays an excellent response to an external magnetic field.

# 3.4 Removal effects of Ag(I) upon Fe<sup>0</sup>/OMC

The impact of the initial concentration of Ag(i) on the adsorption performance of different  $Fe^0/OMC$  materials was investigated, and the results are presented in Figure 9. It can be observed that the adsorption capacity of  $Fe^0/OMC$  increased with the increase in the Ag(i) concentration and reached a nearly constant value at an initial Ag(i) concentration of  $80~mg\cdot L^{-1}$ . Among the  $Fe^0/OMC$  samples,  $Fe^0/OMC$ -1 exhibited the highest adsorption capacity, reaching  $233~mg\cdot g^{-1}$ . As the initial Ag(i) concentration increased, the adsorption process progressed, leading to the gradual occupation of active sites on the surface of  $Fe^0/OMC$ . The superior adsorption capacity of  $Fe^0/OMC$ -1 can be attributed to its larger

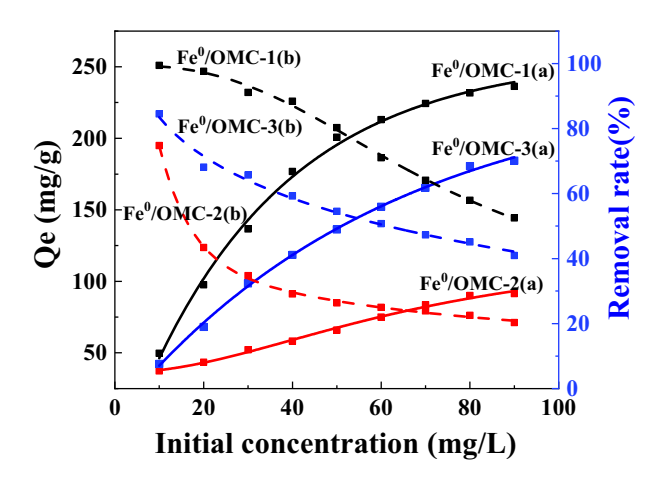
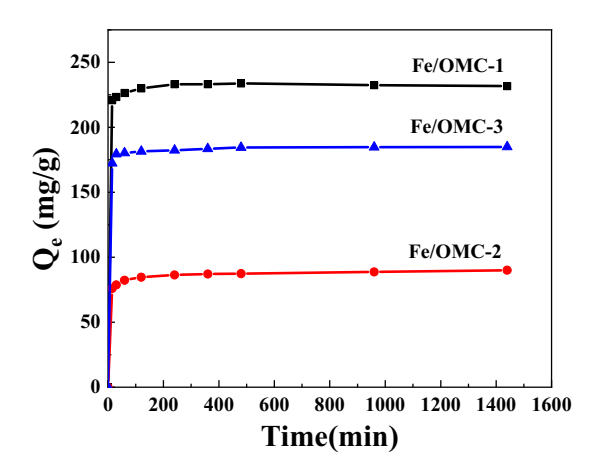


Figure 9: Effect of initial concentrations on adsorption capacity of Ag(i) on  $Fe^0/OMC$ .

specific surface area, which provides more adsorption active sites. Furthermore, the ordered p6mm pore structure of OMC-1 facilitates the entry of Ag(1) into the interior of the pores during the adsorption process, ensuring extensive contact between Ag(1) and the adsorption active sites on the pore surface.

Figure 10 illustrates the impact of magnetic  $Fe^0/OMC$  on the adsorption capacity of Ag(i) at different adsorption times, using an Ag(i) solution with an initial concentration of  $80 \text{ mg} \cdot \text{L}^{-1}$ . It can be observed that the removal rate of magnetic  $Fe^0/OMC$  on Ag(i) is rapid within the first 30 min, with a sharp increase in adsorption capacity during this initial period. After 30 min, the adsorption rate gradually slows down. At an adsorption time of 2 h, the adsorption of



**Figure 10:** Effects of adsorption times on adsorption capacity of Ag(ı) on Fe<sup>0</sup>/OMC.

magnetic Fe<sup>0</sup>/OMC on Ag(I) reaches a dynamic equilibrium, and the adsorption capacity also reaches its maximum.

Throughout the adsorption process, the adsorption rate is remarkably fast, and the adsorption capacity exhibits significant growth within the first 30 min. This can be attributed to the abundant adsorption active sites on the surface of the material and the high concentration of Ag(1) in the solution. As the adsorption experiment progresses, the adsorption active sites provided by Fe<sup>0</sup>/OMC gradually become saturated, leading to a decrease in the adsorption rate of Ag(1). The adsorption capacity tends to level off as the adsorption of Ag(1) reaches its maximum content, signifying the attainment of dynamic equilibrium in the entire adsorption process.

In addition, Table 4 shows the comparison of the adsorption capacity of different adsorbents for Ag(i), and it can be seen that Fe $^0$ /OMC-1 has better adsorption performance.

#### 3.5 Adsorption kinetics

The adsorption kinetics of Ag(i) adsorption by  $Fe^0/OMC$  was investigated to explore the adsorption behavior of Ag(i) in the adsorbent. The adsorption data were analyzed using three kinetic models: the pseudo-first-order model, the pseudo-second-order model, and the intraparticle diffusion model.

Pseudo-first-order model: assuming that the adsorption process was controlled by the diffusion step, the kinetic expression is shown in Eq. (3) [32].

$$\ln(Q_{e1} - Q_t) = \ln Q_{e1} - k_1 t.$$
 (3)

The pseudo-second-order model is based on the assumption that the rate of adsorption is controlled by electron sharing and electron transfer between Fe<sup>0</sup>/OMC and Ag(ı). This process involved the transfer and sharing of electrons between the adsorbent and the adsorbate. The kinetic expression for the pseudo-second-order model is shown in the Eq. (4) [33].

$$\frac{t}{Q_t} = \frac{1}{k_2 Q_{\rm e2}^2} + \frac{t}{Q_{\rm e2}}. (4)$$

Based on the results of the kinetic analysis, an intraparticle diffusion model was employed to investigate the diffusion mechanism of Ag(1) and to identify the rate-limiting step in the adsorption process. The equation for the intraparticle diffusion model is expressed as follows [34]:

$$Q_t = k_i t^{1/2} + C, (5)$$

Table 4: Comparison of adsorption capacity of different adsorbents for Ag(i)

Adsorbents	Adsorption capacity (mg·g <sup>−1</sup> )	Initial concentration of $Ag(I)$ (mg·L <sup>-1</sup> )	Time (min)	Ref.	Adsorbent content
Fe <sup>0</sup> /OMC-1	233	80	120	[Our work]	0.2 g·L <sup>-1</sup>
MnO <sub>2</sub> nanotubes@reduced graphene oxide hydrogel (MNGH)	138.2	200	720	[3]	0.2 g·L <sup>−1</sup>
TU-PVDF	171	107	560	[7]	0.1 g
Fruit shell-derived (SPCs)	115	100	480	[10]	0.2 g·L <sup>-1</sup>
Recycled supercapacitor activated carbon	104.2	2000	1440	[22]	2 g⋅L <sup>-1</sup>
CNS/OH0.5	152	1,080	360	[33]	1 g·L <sup>−1</sup>
TPCFMA	124.3	400	720	[43]	2 g·L <sup>−1</sup>

where  $k_1$  (min<sup>-1</sup>),  $k_2$  (g·(mg·min)<sup>-1</sup>), and  $k_i$  (mg·(g<sup>-1</sup>·min<sup>-0.5</sup>)) represent the rate constants for the pseudo-first-order, pseudo-second-order, and intraparticle diffusion models, respectively.  $Q_t$  (mg·g<sup>-1</sup>) refers to the adsorption capacity at time t, while  $Q_{e1}$  (mg·g<sup>-1</sup>) and  $Q_{e2}$  (mg·g<sup>-1</sup>) denote the adsorption capacities of Ag(i) on Fe<sup>0</sup>/OMC; C (mg·g<sup>-1</sup>) represents the

intercept obtained from the curve derived using the intraparticle diffusion model.

Figure 11 displays the kinetic curves obtained by fitting the data from the adsorption experiments. Figure 11(a) and (b) represent the simulations of the pseudo-first-order model and the pseudo-second-order kinetic model,

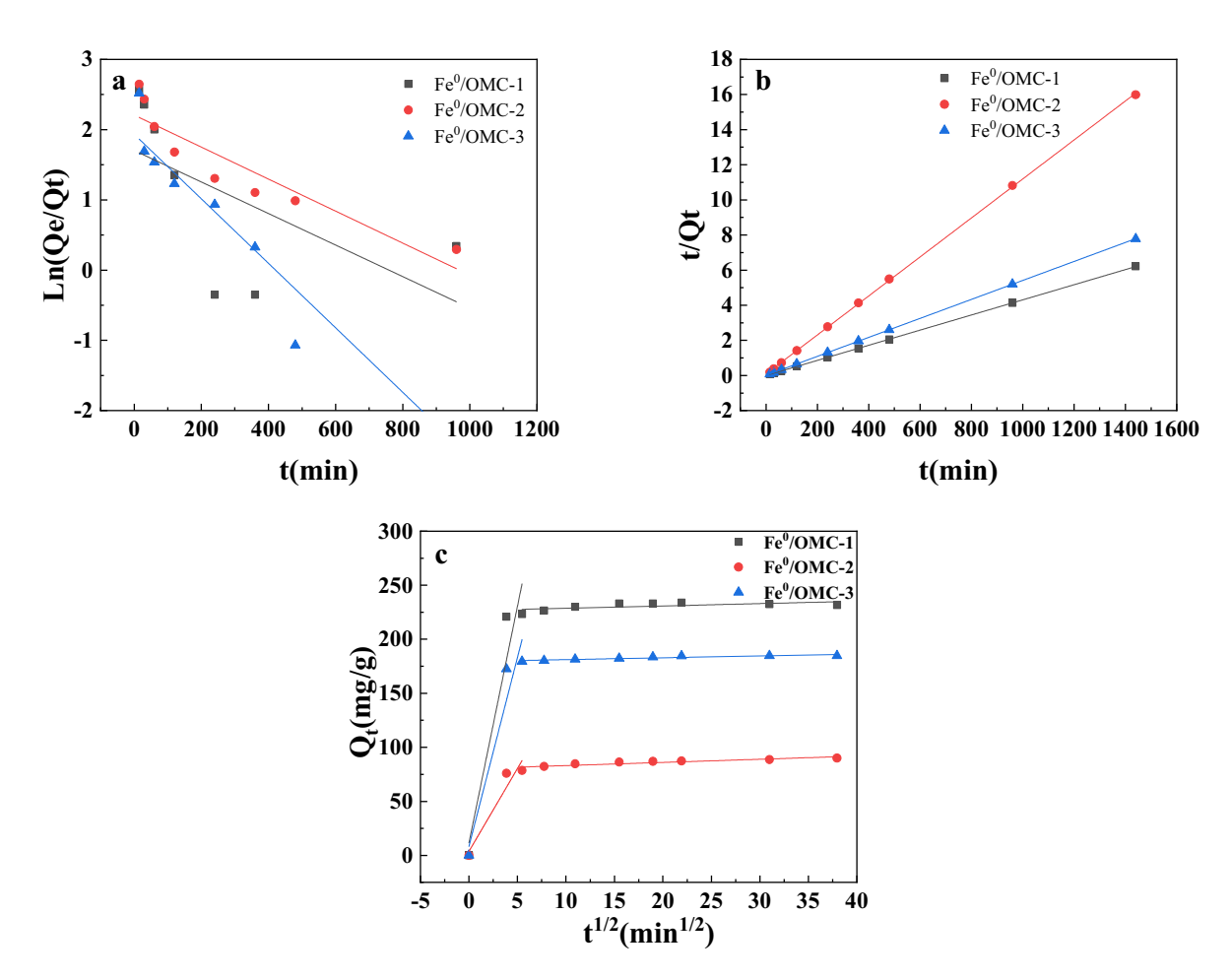


**Figure 11:** Experimental data fitted using (a) quasi-first order, (b) quasi-second order and (c) intraparticle diffusion models for adsorption of Ag(i) by Fe<sup>0</sup>/OMC.

respectively. The comparison presented in Table 4 indicates that the pseudo-second-order kinetic model exhibits a higher  $R^2$  value, suggesting that the adsorption of Ag(i) on  $Fe^0/OMC$  is in agreement with the pseudo-second-order kinetic model. These results suggest that the adsorption process involves electron sharing and electron transfer.

The curves obtained by fitting the intraparticle diffusion model are shown in Figure 11(c), revealing two stages within the overall adsorption process: the surface diffusion stage and the intraparticle diffusion stage. The complete diffusion process of Ag(i) on Fe<sup>0</sup>/OMC primarily involves physical and chemical adsorption, with intraparticle diffusion serving as the rate-controlling step.

## 3.6 Adsorption isotherms

The isothermal adsorption process could describe the interaction between Fe<sup>0</sup>/OMC and Ag(1). Four isothermal adsorption models, Langmuir [35], Freundlich [36], Temkin

[37], and Dubinin-Radushkevich [38], were used to fit the experimental results, respectively. The related expressions were as follows:

Langmuir:

$$\frac{C_{\rm e}}{Q_{\rm e}} = \frac{1}{K_{\rm L}Q_{\rm m}} + \frac{C_{\rm e}}{Q_{\rm m}},$$
 (6)

$$R_{\rm L} = \frac{1}{1 + K_{\rm I} C_0}. (7)$$

Freundlich:

$$\ln Q_{\rm e} = \ln K_{\rm F} + \frac{1}{n} \ln C_{\rm e}. \tag{8}$$

Temkin:

$$Q_{\rm e} = \frac{RT}{b} \ln(K_{\rm T} C_{\rm e}), \tag{9}$$

$$Q_{\rm e} = A + B \ln C_{\rm e},\tag{10}$$

$$A = \frac{RT}{h} \ln K_{\rm T},\tag{11}$$

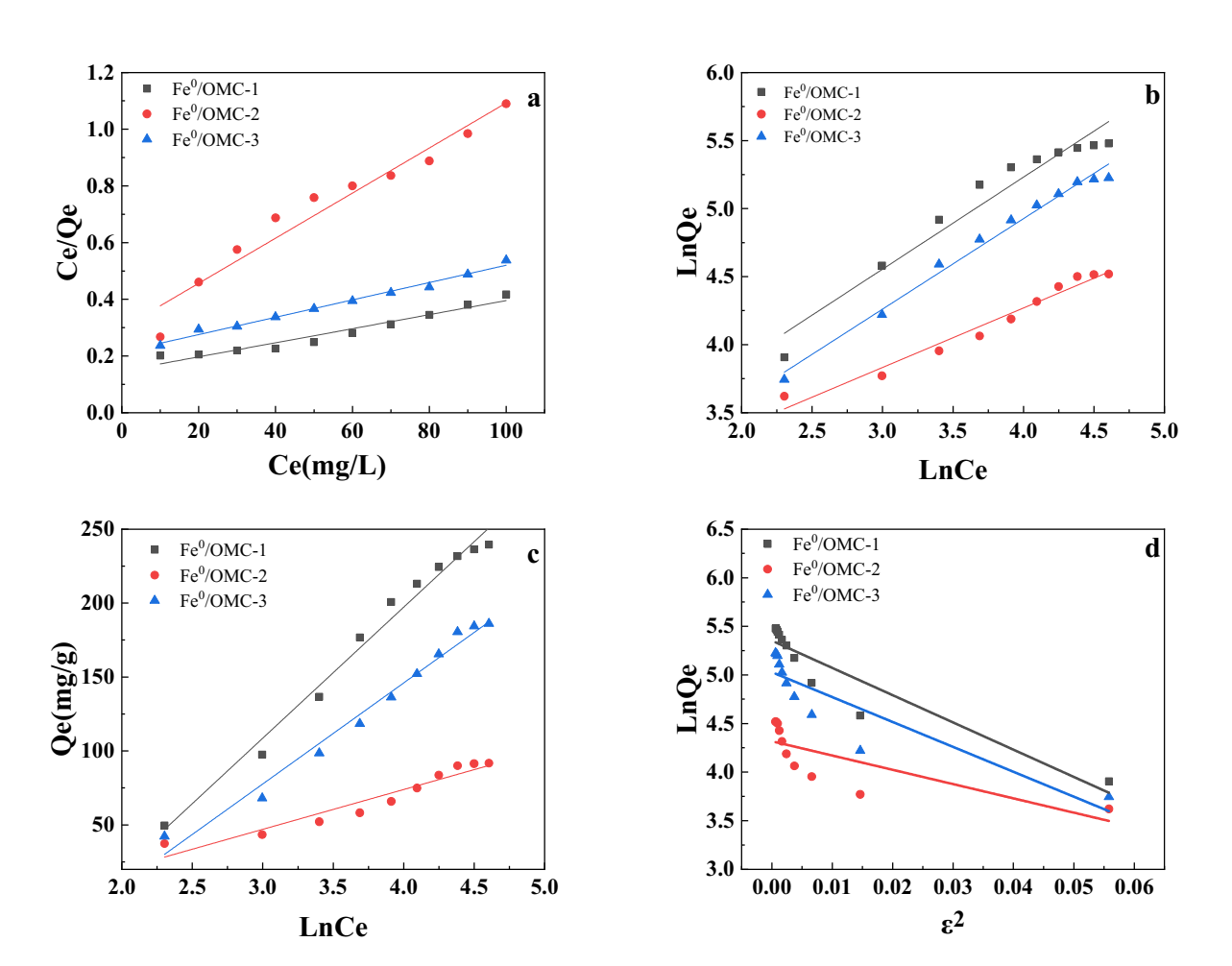


**Figure 12:** Adsorption of Ag(i) Fe<sup>0</sup>/OMC (a) Langmuir isotherm adsorption model, (b) Freundlich isotherm adsorption model, (c) Temkin isotherm adsorption model, and (d) Dubinin-Radushkevich isotherm adsorption model.

$$B=\frac{RT}{b}.$$

Dubinin-Radushkevich:

$$\ln Q_{\rm e} = \ln Q_{\rm m} - \beta \varepsilon^2$$
,

$$\varepsilon = RT \ln \left( 1 + \frac{1}{C_e} \right),$$

$$E = \frac{1}{\sqrt{2\beta}}.$$

- where  $C_{\rm e}$  (mg·L<sup>-1</sup>) represents the equilibrium concentration of the adsorbate and  $Q_{\rm e}$  (mg·g<sup>-1</sup>) represents the equilibrium adsorption capacity;  $Q_{\rm m}$  (mg·g<sup>-1</sup>) refers to the maximum adsorption capacity of the adsorbent.  $K_{\rm L}$ ,  $K_{\rm F}$ , and  $K_{\rm T}$  are equilibrium constants associated with the Langmuir, Freundlich, and Temkin models, respectively. The value of R is the ideal gas constant (8.314 J·(mol·K)<sup>-1</sup>), and T represents the reaction temperature.
  - The experimental data obtained from the Ag(i) adsorption experiments on  $Fe^0/OMC$  were fitted using four

Table 5: Parameters of adsorption kinetics model for adsorption of Ag(i) by Fe<sup>0</sup>/OMC

Models	Parameters	Fe <sup>0</sup> /OMC-1	Fe <sup>0</sup> /OMC-2	Fe <sup>0</sup> /OMC-3
Pseudo-first-order	$R_1^2$	0.36093	0.84707	0.92245
	$K_1$ (min <sup>-1</sup> )	0.0969	0.0740	0.0926
	$Q_{\rm e}$ (exp) (mg·g <sup>-1</sup> )	233	90	185
	$Q_{\rm e}$ (cal) (mg·g <sup>-1</sup> )	229	84	182
	Equation	$\ln(Q_{\rm e} - Q_t) = 1.7037 - 0.00224t$	$\ln(Q_{\rm e} - Q_{\rm t}) = 2.2072 - 0.00228t$	$ln(Q_e - Q_t) = 1.9333 - 0.00459t$
Pseudo-second-order	$R_2^2$	0.9999	0.9998	1
	$Q_{\rm e}$ (exp) (mg·g <sup>-1</sup> )	233	90	185
	$Q_{\rm e}$ (cal) (mg·g <sup>-1</sup> )	232	90	185
	$K_2 (g \cdot (mg \cdot min)^{-1})$	0.0478	0.00136	0.00272
	Equation	$t/Q_t = 0.00431t + 0.000389$	$t/Q_t = 0.0111t + 0.09024$	$t/Q_t = 0.0054t + 0.0107$
Intraparticle diffusion	$R_{i1}^2$	0.9993	0.9999	0.7415
	$R_{i2}^2$	0.2639	0.9008	0.8190
	$k_{i1}$ (mg·(g <sup>-1</sup> ·min <sup>-0.5</sup> ))	1.451	1.645	1.895
	$k_{i2} \text{ (mg} \cdot (\text{g}^{-1} \cdot \text{min}^{-0.5}))$	0.122	0.225	0.152
	Equation <sub>i1</sub>	$Q_t = 1.451t^{1/2} + 215.277$	$Q_t = 1.645t^{1/2} + 69.619$	$Q_t = 1.895t^{1/2} + 166.564$
	Equation <sub>i2</sub>	$Q_t = 0.122t^{1/2} + 229.040$	$Q_t = 0.225t^{1/2} + 82.043$	$Q_t = 0.152t^{1/2} + 179.950$

(12)

(13)

(14)

(15)

Table 6: Adsorption isotherm model parameters for adsorption of Ag(ı) on Fe<sup>0</sup>/OMC

Models	Constants	Fe <sup>0</sup> /OMC-1	Fe <sup>0</sup> /OMC-2	Fe <sup>0</sup> /OMC-3
Langmuir	$Q_{\text{max}}$ (mg·g <sup>-1</sup> )	403	125	326
	$K_{L}$ (L·mg <sup>-1</sup> )	0.0000418	0.000213	0.0000438
	$R^2$	0.94941	0.95148	0.98723
	Equation	$C_{\rm e}/Q_{\rm e} = 0.147 + 0.00248C_{\rm e}$	$C_{\rm e}/Q_{\rm e} = 0.297 + 0.00795C_{\rm e}$	$C_{\rm e}/Q_{\rm e} = 0.214 + 0.00306C_{\rm e}$
Freundlich	$K_{\rm F}$ (mg·g <sup>-1</sup> )	12.503	12.441	9.641
	N (mg·L <sup>-1</sup> )	1.479	2.288	1.504
	$R^2$	0.94653	0.96914	0.98727
	Equation	$\ln Q_{\rm e}$ = 2.526 + 0.676 $\ln C_{\rm e}$	$\ln Q_{\rm e}$ = 2.521 + 0.437 $\ln C_{\rm e}$	In $Q_e$ = 2.266 + 0.665 In $C_e$
Temkin	$K_{\rm T}$ (L·g <sup>-1</sup> )	0.170	0.286	0.155
	<i>B</i> (J·mol <sup>−1</sup> )	27.987	92.135	36.296
	$R^2$	0.98453	0.9263	0.98136
	Equation	$Q_{\rm e}$ = 88.571 ln $C_{\rm e}$ – 157.055	$Q_{\rm e}$ = 26.904 In $C_{\rm e}$ – 33.694	$Q_{\rm e}$ = 68.294 ln $C_{\rm e}$ – 127.184
Dubinin-Radushkevich	$Q_{\rm max}$ (mg·g <sup>-1</sup> )	211	75	152
	$B \text{ (mol}^2 \cdot \text{kJ}^{-2})$	28.486	14.698	25.626
	E (kJ·mol <sup>-1</sup> )	0.132	0.184	0.140
	$R^2$	0.8812	0.59291	0.79348
	Equation	In $Q_e = 5.352 - 28.486\epsilon^2$	In $Q_e = 4.318 - 14.698\epsilon^2$	In $Q_e = 5.028 - 25.626\varepsilon^2$

14 — Wenjuan Zhang et al. DE GRUYTER

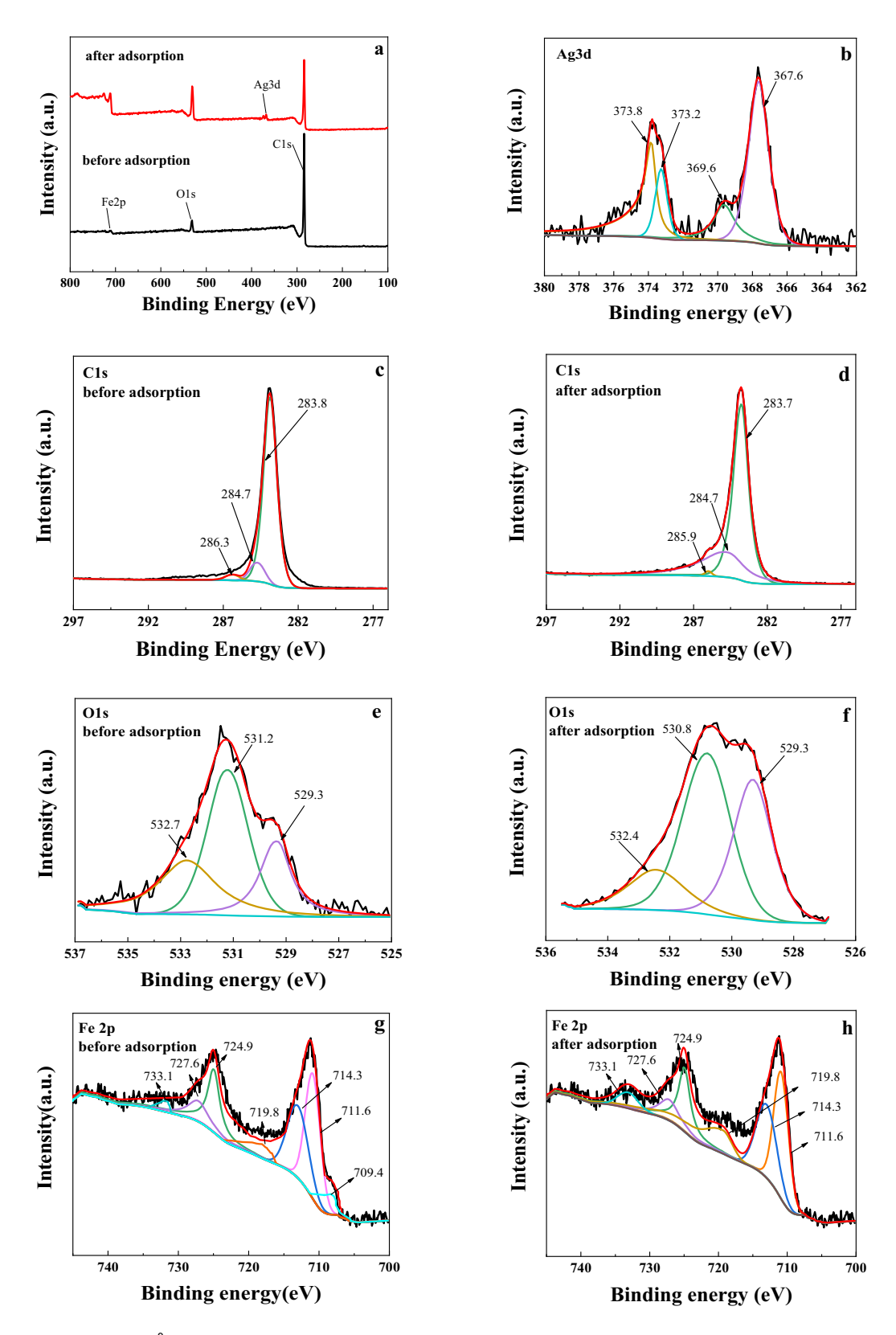


**Figure 13:** XPS spectra of (a)  $Fe^0$ /OMC-1 before and after adsorption of Ag(i). High resolution spectra of (b) Ag 3d after adsorption of Ag(i). High resolution spectra of (c and d) C 1s, (e and f) O 1s and (g and h) Fe 2p for  $Fe^0$ /OMC-1 before and after adsorption of Ag(i).

isothermal adsorption models: Langmuir, Freundlich, Temkin, and Dubinin-Radushkevich. The results of the fitting are presented in Figure 12, and the fitted parameters are listed in Table 5. Among the four models, the Freundlich isothermal adsorption model provides a better simulation of the adsorption data. This suggests that the adsorption process involves multilayer adsorption on a heterogeneous surface (Table 6).

#### 3.7 Adsorption mechanism

To further understand the adsorption mechanism of Ag(1) from solution by magnetic Fe<sup>0</sup>/OMC-1, the chemical compositions of the material before and after adsorption of Ag(1) by Fe<sup>0</sup>/OMC-1 were characterized by XPS. Figure 13(a) shows a full scan of Fe/OMC-1 before and after adsorption. The spectrum of the Ag(1)-adsorbed material (Figure 13(b)) reveals an additional Ag 3d peak, corroborating the existence of elemental Ag on Fe<sup>0</sup>/OMC. XPS spectrum of the regions for C 1s, O 1s, and Fe 2p of the Fe<sup>0</sup>/OMC before and after adsorption of Ag(I) are shown in Figure 13(c-h).

A high-resolution scan of Ag(I) adsorbed Fe/OMC shows two large characteristic peaks of Ag 3d as shown in Figure 13(b). By splitting and fitting the characteristic peaks, two characteristic peaks of 369.6 and 373.2 eV representing Ag(1) and two characteristic peaks of 367.6 and 373.8 eV representing Ag singlet could finally be obtained. This result shows the coexistence of Ag(I) and Ag after adsorption. After adsorption, Ag(i) and Ag accounted for 38% and 62% of the Ag in Fe<sup>0</sup>/OMC-1, respectively, indicating that Ag(i) was partially reduced through redox adsorption of Fe<sup>0</sup>/OMC. The C 1s spectra (Figure 13(c) and (d)) for the material before and after adsorption of Ag(I) showed little change, indicating that the features of the skeleton of Fe/OMC are very stable. As shown in Figure 13(e), the O 1s peaks can be decomposed into four components originating from -OH (around 531.2 eV), O<sup>2-</sup> (around 529.3 eV), and O-O=C (around 532.7 eV). The O<sup>2-</sup> at 529.3 eV (Figure 13(f)) belonged to the Fe-O in the Fe<sup>0</sup>/OMC-1 that was oxidized to Fe<sub>3</sub>O<sub>4</sub> characteristic peaks [39,40]. Figure 13(g) and (h) shows the high-resolution spectra of Fe 2p. Before adsorption, 709.4 eV corresponds to the characteristic peak of Fe<sup>0</sup> [41]; 711.6, 724.9 and 727.6 eV can be attributed to the  $Fe^{2+}$ ; 714.3, 719.8, and 733.1 eV correspond to the characteristic peaks of Fe<sup>3+</sup> [42]. After adsorption, the characteristic peak area of Fe<sup>0</sup> decreased while the characteristic peak area of Fe<sup>3+</sup> increased, which was due to the partial involvement of Fe<sup>0</sup> in the redox reaction to generate iron oxides during the adsorption process, while reducing Ag(1) to Ag. The above results indicated that the magnetic Fe/OMC-1 has

undergone not only physical adsorption but also redox reactions during the adsorption of Ag(I).

#### 4 Conclusion

The successful synthesis of three OMC materials with different structures was achieved using a soft-template induction method. These materials were then loaded with Fe<sup>0</sup> through impregnation and carbon thermal in situ reduction method. The specific surface area and pore volume of the Fe<sup>0</sup>/OMC decreased after Fe loading, but the presence of Fe resulted in increased Fe-containing chemical bonding adsorption active sites on the material surface. These functional groups were found to be beneficial for the adsorption capacity of the materials.

The adsorption process of Ag(1) by the Fe<sup>0</sup>/OMC-1 composite was well-described by the pseudo-second-order kinetic model and Freundlich isotherm adsorption model. This suggests that the adsorption of Ag(1) occurred through a multilayer adsorption on a heterogeneous surface, and the presence of Fe<sup>0</sup> exhibited a synergistic effect on the adsorption of Ag(I). X-ray photoelectron spectroscopy (XPS) analysis supported this mechanism by revealing that the adsorption of Ag (1) by Fe<sup>0</sup>/OMC involved both physical adsorption through active sites on the material surface and a redox reaction facilitated by the loaded Fe<sup>0</sup>. Ultimately, Ag(I) was adsorbed onto the surface of Fe<sup>0</sup>/OMC in the form of Ag(1) and Ag species.

Acknowledgments: The authors would like to acknowledge the support of the Major Science and Technology Project of Gansu Province (22ZD6GA008) for paying the Article Processing Charges (APC) of this publication.

**Funding information:** This work was supported by the Major Science and Technology Project of Gansu Province (Grant No.22ZD6GA008); National Natural Science Foundation of China (51703088 and 52262013); Key laboratory of polymer materials opening fund project in 2018 (KF-18-03); Hongliu youth fund of Lanzhou university of technology (061805); Natural Science Foundation of Gansu Province (21JR7RA259); Gansu Province for young doctor (2021QB-048). We thank State Key Laboratory for Advanced Processing and Recycling of Nonferrous Metals in Lanzhou University of Technology, Lanzhou, Gansu Province.

Author contributions: Wenjuan Zhang: conceptualization, methodology, writing - review and editing, and supervision. Yuheng Li: writing - original draft and formal analysis. Mengyu Ran: validation and data curation. Youliang Wang: supervision. Yezhi Ding: writing – review and editing. Bobo Zhang: data curation. Qiancheng Feng: validation. Qianqian Chu: funding acquisition. Yongqian Shen: supervision. Wang Sheng: supervision and data curation. All authors have accepted responsibility for the entire content of this manuscript and approved its submission.

**Conflict of interest:** The authors state no conflict of interest.

**Data availability statement:** The datasets generated and/ or analyzed during the current study are available from the corresponding author on reasonable request.

#### References

- [1] Simona, S., E. Abdelhamid, M. Rita, and J. R. Nicole. Aptamers functionalized metal and metal oxide nanoparticles: Recent advances in heavy metal monitoring. *TrAC Trends in Analytical Chemistry*, Vol. 157, 2022, id. 116748.
- [2] El Bahgy, H. E. K., H. Elabd, and R. M. Elkorashey. Heavy metals bioaccumulation in marine cultured fish and its probabilistic health hazard. *Environmental Science and Pollution Research*, Vol. 28, 2021, pp. 41431–41438.
- [3] Zeng, T., Y. Yu, Z. Li, J. Zuo, Z. Kuai, Y. Jin, et al. 3D MnO<sub>2</sub> nanotubes@reduced graphene oxide hydrogel as reusable adsorbent for the removal of heavy metal ions. *Materials Chemistry and Physics*, Vol. 231, 2019, pp. 105–108.
- [4] Zhuo, X., M. Henriksen-Lacey, D. Jimenez de Aberasturi, A. Sánchez-Iglesias, and L. M. Liz-Marzán. Shielded silver nanorods for bioapplications. *Chemistry of Materials*, Vol. 32, No. 13, 2020, pp. 5879–5889.
- [5] Tortella, G. R., O. Rubilar, N. Durán, M. C. Diez, M. Martínez, J. Parada, et al. Silver nanoparticles: Toxicity in model organisms as an overview of its hazard for human health and the environment. *Journal of Hazardous Materials*, Vol. 390, 2020, id. 121974.
- [6] Liu, X. and Y. Wang. Activated carbon supported nanoscale zerovalent iron composite: Aspects of surface structure and composition. *Materials Chemistry and Physics*, Vol. 222, 2019, pp. 369–376.
- [7] Liu, P., X. Wang, L. Tian, B. He, X. Lv, X. Li, et al. Adsorption of silver ion from the aqueous solution using a polyvinylidene fluoride functional membrane bearing thiourea groups. *Journal of Water Process Engineering*, Vol. 34, 2020, id. 101184.
- [8] Herman, P., D. Pércsi, T. Fodor, L. Juhász, Z. Dudás, Z. E. Horváth, et al. Selective and high capacity recovery of aqueous Ag(i) by thiol functionalized mesoporous silica sorbent. *Journal of Molecular Liquids*, Vol. 387, No. 1, 2023, id. 122598.
- [9] Al-Anber, M. A., M. Al Ja'afreh, I. F. Al-Momani, A. K. Hijazi, D. Sobola, S. Sagadevan, et al. Loading of silver(i) ion in L-cysteine-functionalized silica gel material for aquatic purification. *Gels*, Vol. 9, No. 11, 2023, id. 865.
- [10] Fan, J., L. Duan, X. Zhang, Z. Li, P. Qiu, Y. He, et al. Selective adsorption and recovery of silver from acidic solution using biomass-derived sulfur-doped porous carbon. ACS Applied Materials & Interfaces, Vol. 15, 2023, pp. 40088–40099.
- [11] Mu, Y., Z. Ai, and L. Zhang. Phosphate shifted oxygen reduction pathway on Fe@Fe<sub>2</sub>O<sub>3</sub> core-shell nanowires for enhanced reactive oxygen species generation and aerobic 4-chlorophenol

- degradation. *Environmental Science and Technology*, Vol. 51, No. 14, 2017, pp. 8101–8109.
- [12] Bae, S., R. N. Collins, T. D. Waite, and K. Hanna. Advances in surface passivation of nanoscale zerovalent iron (NZVI): A critical review. *Environmental Science and Technology*, Vol. 52, No. 21, 2018, pp. 12010–12025.
- [13] Dai, Y., Y. Hu, B. Jiang, J. Zou, G. Tian, and H. Fu. Carbothermal synthesis of ordered mesoporous carbon-supported nano zerovalent iron with enhanced stability and activity for hexavalent chromium reduction. *Journal of Hazardous Materials*, Vol. 309, 2016, pp. 249–258.
- [14] Wang, J., G. Liu, C. Zhou, T. Li, and J. Liu. Synthesis, characterization and aging study of kaolinite-supported zero-valent iron nanoparticles and its application for Ni(II) adsorption. *Materials Research Bulletin*, Vol. 60, 2014, pp. 421–432.
- [15] Okonji, S. O., G. Achari, and D. Pernitsky. Removal of organoselenium from aqueous solution by nanoscale zerovalent iron supported on granular activated carbon. *Water*, Vol. 14, No. 6, 2022, id. 987.
- [16] Guo, Y., Y. Zhao, T. Yang, B. Gong, and B. Chen. Highly efficient nano-Fe/Cu bimetal-loaded mesoporous silica Fe/Cu-MCM-41 for the removal of Cr(VI): Kinetics, mechanism and performance. *Journal of Hazardous Materials*, Vol. 418, 2021, id. 126344.
- [17] Liu, Z., F. Zhang, S. K. Hoekman, T. Liu, C. Gai, and N. Peng. Homogeneously dispersed zerovalent iron nanoparticles supported on hydrochar-derived porous carbon: Simple, in situ synthesis and use for dechlorination of PCBs. ACS Sustainable Chemistry & Engineering, Vol. 4, No. 6, 2016, pp. 3261–3267.
- [18] Teng, W., J. Fan, W. Wang, N. Bai, R. Liu, Y. Liu, et al. Nanoscale zerovalent iron in mesoporous carbon (nZVI@C): stable nanoparticles for metal extraction and catalysis. *Journal of Materials Chemistry A: Materials for Energy and Sustainability*, Vol. 5, 2017, pp. 4478–4485.
- [19] Sun, X., J. Fang, R. Xu, M. Wang, H. Yang, Z. Han, et al. Nanoscale zero-valent iron immobilized inside the mesopores of ordered mesoporous carbon by the "two solvents" reduction technique for Cr(VI) and As(V) removal from aqueous solution. *Journal of Molecular Liquids*, Vol. 315, 2020, id. 113598.
- [20] Lin, Y. and J. Chen. Magnetic mesoporous Fe/carbon aerogel structures with enhanced arsenic removal efficiency. *Journal of Colloid and Interface Science*, Vol. 420, 2014, pp. 74–79.
- [21] Yuan, P., J. Liu, Y. Li, Y. Fan, G. Shi, H. Liu, et al. Effect of pore diameter and structure of mesoporous sieve supported catalysts on hydrodesulfurization performance. *Chemical Engineering Science*, Vol. 111, 2014, pp. 381–389.
- [22] Wu, F., T. Zhao, Y. Yao, T. Jiang, B. Wang, and M. Wang. Recycling supercapacitor activated carbons for adsorption of silver(i) and chromium (VI) ions from aqueous solutions. *Chemosphere*, Vol. 238, 2020, id. 124638.
- [23] Du, Y., T. Liu, B. Yu, H. Gao, P. Xu, J. Wang, et al. The electromagnetic properties and microwave absorption of mesoporous carbon. *Materials Chemistry and Physics*, Vol. 135, 2012, pp. 884–891.
- [24] Liu, S. and S. C. Chen. Stepwise synthesis, characterization, and electrochemical properties of ordered mesoporous carbons containing well-dispersed Pt nanoparticles using a functionalized template route. *Journal of Solid State Chemistry*, Vol. 184, No. 9, 2011, pp. 2420–2427.
- [25] Li, K., Y. Zhou, J. Li, and J. Liu. Soft-templating synthesis of partially graphitic Fe-embedded ordered mesoporous carbon with rich micropores from bayberry kernel and its adsorption for Pb(II) and Cr(III). Journal of the Taiwan Institute of Chemical Engineers, Vol. 82, 2018, pp. 312–321.

- [26] Wei, J., Z. Sun, W. Luo, Y. Li, A. A. Elzatahry, A. M. Al-Enizi, et al. New insight into the synthesis of large-pore ordered mesoporous materials. Journal of the American Chemical Society, Vol. 139, No. 5, 2017, pp. 1706-1713.
- [27] Meng, Y., D. Gu, F. Zhang, Y. Shi, H. Yang, Z. Li, et al. Ordered mesoporous polymers and homologous carbon frameworks: Amphiphilic surfactant templating and direct transformation. Angewandte Chemie International Edition, Vol. 44, 2005, pp. 7053-7059.
- [28] Deng, Y., T. Yu, Y. Wan, Y. Shi, Y. Meng, D. Gu, et al. Ordered mesoporous silicas and carbons with large accessible pores templated from amphiphilic deblock copolymer poly(ethylene oxide)-bpolystyrene. Journal of the American Chemical Society, Vol. 129, 2007, pp. 1690-1697.
- [29] Kim, Y. J., M. I. Kim, C. H. Yun, J. Y. Chang, C. R. Park, and M. J. Inagaki. Comparative study of carbon dioxide and nitrogen atmospheric effects on the chemical structure changes during pyrolysis of phenol-formaldehyde spheres. Journal of Colloid and Interface Science, Vol. 274, No. 2, 2004, pp. 555-562.
- [30] Qian, L., X. Shang, B. Zhang, W. Zhang, A. Su, Y. Chen, et al. Enhanced removal of Cr(vI) by silicon rich biochar-supported nanoscale zero-valent iron. Chemosphere, Vol. 215, 2019, pp. 739-745.
- [31] Jiaman, L. I., D. A. I. Yexin, L. I. Yuwei, L. I. U. Fang, Z. H. A. O. Chaocheng, and W. A. N. G. Yongqiang. Adsorption of p-Nitrophenol from aqueous solution by mesoporous carbon and its Fe-modified materials. Acta Petrolei Sinica (Petroleum Processing Section), Vol. 35, No. 1, 2019, pp. 136-145.
- [32] Ho, Y. S. and G. McKay. The sorption of lead(II) ions on peat. Water Research, Vol. 33, No. 2, 1999, pp. 580-584.
- [33] Song, X., P. Gunawan, R. Jiang, S. S. J. Leong, K. Wang, and R. Xu. Surface activated carbon nanospheres for fast adsorption of silver

- ions from aqueous solutions. Journal of Hazardous Materials, Vol. 194, 2011, pp. 162-168.
- [34] Weber, W. J. Jr and J. C. Morris. Kinetics of adsorption on carbon from solution. Journal of the Sanitary Engineering Division, Vol. 1, No. 2, 1963, pp. 1-2.
- [35] Langmuir, I. Vapor pressures, evaporation, condensation and adsorption. Journal of the American Chemical Society, Vol. 68, No. 6, 1932, pp. 370-373.
- [36] Freundlich, H. Over the adsorption in solution. Journal of Physical Chemistry, Vol. 57, 1906, pp. 385-471.
- Roginsky, S. Z. and Y. B. Zeldovich. Die katalische oxidation von kohlenmonoxyd auf mangandioxyd. Acta Physiochimica URSS, Vol. 1, 1934, pp. 554-594.
- [38] Dubinin, M. M. and L. V. Radushkevich. Equation of the characteristic curve of the activated charcoal. Chemisches Zentralblatt, Vol. 1, 1947, pp. 875-890.
- [39] Zhang, Y. Preparation of polymer coated magnetic nanomaterials and their application for adsorption and separation. Dissertation. Ludong University, Shandong, 2014.
- [40] Blum, R., S. Reiche, and X. C. Zhao. Reactivity of mesoporous carbon against water - an in-situ XPS study. Carbon, Vol. 77, 2014, pp. 175-183.
- Sun, Y. P., X. Q. Li, J. Cao, W. X. Zhang, and H. P. Wang. Characterization of zero-valent iron nanoparticles. Advances in Colloid and Interface Science, Vol. 120, No. 1-3, 2006, pp. 47-56.
- [42] Wang, X. Study on nanoscale zero-valent iron and its modified bimetallic Pd/Fe materials in nitrate reduction. Dissertation. Chongging Technology and Business University, Chongqing, 2021.
- Zhao, W., Y. Huang, R. Chen, H. Peng, Y. Liao, and Q. Wang. Facile preparation of thioether/hydroxyl functionalized polyhedral oligomeric silsesquioxanes hybrid polymer for ultrahigh selective adsorption of silver(i) ions. Reactive & Functional Polymers, Vol. 163, 2021, id. 104899.